Chapter 3
Cloisite 20A Based Polyaniline Nanocomposites for Nitrogen Dioxide (No_2) Gas Sensors

Muktikanta Panigrahi [1, *], Basudam Adhikari [1]

[1] Materials Science Centre, Indian Institute of Technology, Kharagpur, West Bengal, India

*Corresponding author: muktikanta2@gmail.com

Abstract

Compacted polyaniline (PANI)/Layered silicate nanocomposites have been successfully prepared by simple *in situ*, *core-shell*, and *ex situ* polymerization routes using AnHCl as a predecessor through chemical oxidation method. The structure, chemical groups, electronic transition and properties were investigated by XRD, SEM, HRTEM, UV Visible, DC electrical conductivity, TGA, and DSC. The XRD results reveals that HCl-treated Cloisite 20A, and PANI-ES/Cloisite 20A nanocomposites are delaminated. Flake-like morphologies were observed in Cloisite 20A and HCl-treated Cloisite 20A, whereas different rate of compacted fibrous morphologies of prepared PANI-ES/Cloisite 20A nanocomposites were observed as evident from SEM images. The Si-O FTIR band position does not change even after HCl treatment of Cloisite 20A, but different FTIR peaks positions of PANI-ES/Cloisite 20A nanocomposites were shifted from pure PANI-ES peaks after using Cloisite 20A nanoclays. UV-Visible spectra indicated the increment of charge carrier within the PANI-ES/Cloisite 20A nanocomposites compared to the pure one. The prepared nanohybrids showed significantly improved thermal property compared to pristine PANI-ES as clear from TGA and DSC analysis. The highest DC electronic conductivity of nanocomposite prepared by *core-shell* route is found to be 5.12 S/cm using linear four probe techniques. In addition, the charge transport mechanism was understood with and without loading Cloisite 20A in PANI-ES. The conductivity data supported the temperature-dependence relationship $\sigma(T) = \sigma 0.\exp[-To/T)^{1/4}]$ and followed characteristic of three-dimensional variable-range hopping (3D–VRH) mechanism. In addition, we were discussed the response of Nitrogen dioxide (NO_2) gas with polyaniline based sensor materials.

Keywords: PANI-ES, Nanofibers, Delamination, Enthalpy, Electrical conductivity, VRH mechanism

Muktikanta Panigrahi & Basudam Adhikari, *Fundamentals on Polyaniline based Composites*
https://doi.org/10.34256/ioriip2123

1. Introduction

Conducting polymers have attracted much more attention of scientific community in recent decades because of their prospective application in different fields such as antistatic shielding, light emitting diodes, supercapacitors, rechargeable batteries, sensors, corrosion inhibitors and artificial muscles [1-6]. Among the known conducting polymers, PANI has been extensively studied due to its ease of synthesis *via* chemical and electrochemical routes, good environmental stability, unique acid-base doping-dedoping, oxidation reduction chemistry and low-cost synthesis [7-9]. However, the electrical and physical properties of PANI are not satisfactory for practical purpose. To solve this, development of polymer nanocomposites is one of the effective ways to improve material performance.

Among the large number of layered solids, clay minerals especially the members of smectite group are most suitable for the reinforcement of polymer matrix. Organically modified layered silicates (OMLS) nanoclays have been used to prepare the cost-effective polymer nanocomposite because of their unique structure, reactivity combined with their high strength, stiffness and high aspect ratio of each clay platelet [10,11]. And also layered structured (2:1 smectite minerals) possess a high negative charge density, high anisotropy, which make them of great capacity for surface adsorption and also catalytic activity in organic reactions. The structure of smectite hydrophobic clays (2:1 type) minerals, has received great attention when the PANI confinement is desirable [10]. Chemical structure of smectite clay minerals forms by sandwiching an $MO_4(OH)_2$ octahedron sheet between two MO_4 tetrahedron sheets producing layers designated by T:O:T which consists of nanometer thick layers. The octahedral sites are occupied by ions such as aluminium, magnesium and iron; while the tetrahedral site accommodates silicon and aluminium. The overall negative charge of individual layer assumes to have a parallel orientation and the electric charge is neutralized by the presence of exchangeable hydrated positive ion in the interlayer space [10-13]. In the present work, Cloisite 20A was chosen as reinforcing filler because the platelets are generally surface modified with surfactants to allow complete dispersion, provide miscibility, *i.e.*, compatibility with the polymer system; and improve the thermal stability and compactness of polymer chains for which they were designed.

There are several literature reports on the preparation of PANI-clay based nanocomposites with different weight percentages of dispersion [14-17].The majorities of reports show *in situ* polymerization technique to prepare clay based intercalated/exfoliated nanocomposites [14-17]. In addition, emulsion polymerization method was employed to prepare the clay based nanocomposites [18]. Both intercalated and exfoliated conducting polymer nanocomposites show better properties such as stiffness, strength and barrier with few weight percentage of inorganic-organic clay content [14-17]. It is rationalized that higher is the degree of exfoliation between polymer and inorganic-organic hybrid nanocomposites, the greater is the increment of materials properties. Recently, Yeh ***et al.*** [19] have reported that polyaniline clay-based nanocomposites with exfoliated silicate layers are

successfully prepared using organically modified clay.

Different spectroscopic analyses such as XRD, FTIR, and UV-Visible *etc.* were used to characterize the prepared layered silicate composite materials [14-17]. Particularly, Raman spectroscopic analysis has been modest discovered to examine the nature of these composite materials [20]. In this paper, we have reported the synthesis of PANI-ES, PANI-ES/Cloisite 20A nanocomposites from aniline hydrochlorides (AnHCl) *via in situ* polymerization route. We analyzed the effect of 4 wt% Cloisite 20A nanoclays on nanostructure, crystallinity, charge transfer spectra, thermal stability, and DC conductivity at room temperature as well as temperature dependent (with and without field) in PANI-ES chains.

2. Experimental Section

2.1. Synthesis of PANI-ES/Cloisite 20a (4 Wt%) Nanocomposites by *In Situ* Route.

PANI-ES was synthesized by a simple chemical oxidation polymerization technique from AnHCl (monomer) at room temperature. For this synthesis, three different types of solutions were required to complete the polymerization. Therefore, Solution 1 was prepared by adding 50 mL of 1 (M) HCl and 2.59 g (0.03 moles) of AnHCl and was stirred to 1 h. Solution 2 was also prepared by mixing 50 mL of 1 (M) HCl and 10.26 g (0.045 moles) ammonium perdisulphate (APS). Solution 2 was added drop wise to the solution 1 to form solution 3.

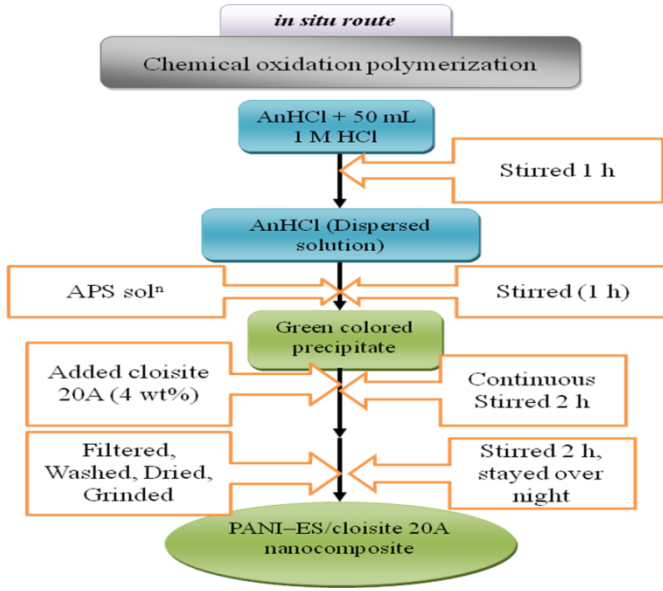

Scheme 1. Summary of the *in-situ* route synthesized PANI-ES/Cloisite 20A (4 wt%) nanocomposites

During this addition, the color of solution 3 changed from slight yellowish to blue to green color. This was observed that the polymerization was continued under constant stirring (2 h).[20] Then, 0.1036 g (4 wt%) of Cloisite 20A was added on solution 3 by constant stirring and kept for 12 h for complete reaction and polymerization. The resulting products were filtered and washed with 1 (M) HCl, deionizer water, diethyl ether and dried under vacuum at 60 °C for 6 h. For comparison, pure PANI-ES powders were prepared under conditions similar to those mentioned above up to addition of Cloisite 20A. Summary of the *in situ* route to synthesized PANI-ES/Cloisite 20A nanomaterials is shown as flow chart in **Scheme 1.**

2.2. Synthesis Of PANI-ES/Cloisite 20a (4 Wt%) Nanocomposites by *Ex Situ* Polymerization Process.

In this process, PANI-ES/Cloisite 20A (4 wt%) nanocomposites were synthesized by a simple *ex situ* polymerization route using AnHCl as precursor at room temperature.[21] The synthesis procedure was slightly modified in the procedure for preparation of nanocomposite. Generally, two type of prepared solutions were required for synthesis of PANI-ES/Cloisite 20A (4 wt%) nanocomposites. Accordingly, solution A was prepared by taking 50 mL of 1 (M) HCl and 4 wt% Cloisite 20A. It was stirred continuously and followed by the addition of 2.59 g of AnHCl for 1 h to form dispersed solution. Solution B was also prepared by mixing 50 mL of 1 (M) HCl and 10.26 g (0.045 moles) of APS as oxidant.

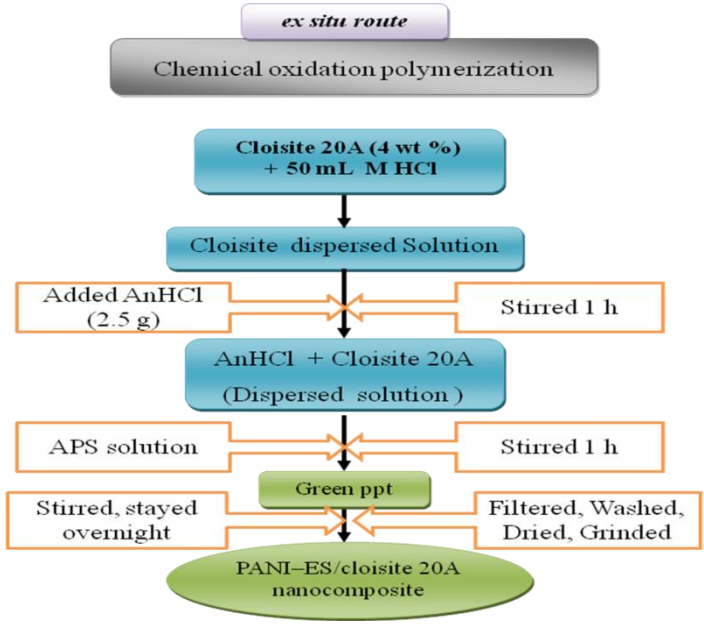

Scheme 2. The flow chart for *ex situ* route synthesized PANI-ES/Cloisite 20A (4 wt%) nanocomposites

Solution B was added drop wise to the solution A to 1 h and the polymerization is carried out. During this addition, the color of the solution changed from slight blackish to blue to green color and then deep green color. It may believe that the polymerization was carried out under constant stirring for 2 h.[21] The obtained dispersion was kept for overnight for complete reaction and polymerization. The resulting dispersion was filtered and washed with 1(M) HCl, deionized (DI) water, diethyl ether and dried under vacuum at 60 °C for 6 h to get HCl doped PANI-ES/Cloisite 20A (4 wt%) nanocomposites. The flow chart for *ex situ* route synthesis of PANI-ES/Cloisite 20A (4 wt%) nanocomposites is shown in **Scheme 2**.

2.3. Synthesis Of PANI-Es/Cloisite 20a (4 Wt%) Nanocomposites by *CORE-SHELL* Polymerization Process.

In a typical synthesis route, PANI-ES/Cloisite 20Ananocomposites was synthesized by a simple *core-shell* polymerization route at room temperature using AnHCl as starting materials. The details synthesis procedure is followed as described in the literature.[22] For this synthesis, two types of prepared solutions such as Cloisite 20A dispersed in monomer solution (dispersed solution) and oxidant (APS) solution were needed. Accordingly, dispersed solution consisted of 50 mL 1 (M) HCl and AnHCl (2.59 g) in which 4 wt% Cloisite 20A was dispersed. This dispersion was stirred continuously for 1 h. Oxidant solution was also prepared by taking 50 mL of 1 (M) HCl and 10.26 g (0.045 moles) of APS as oxidant.

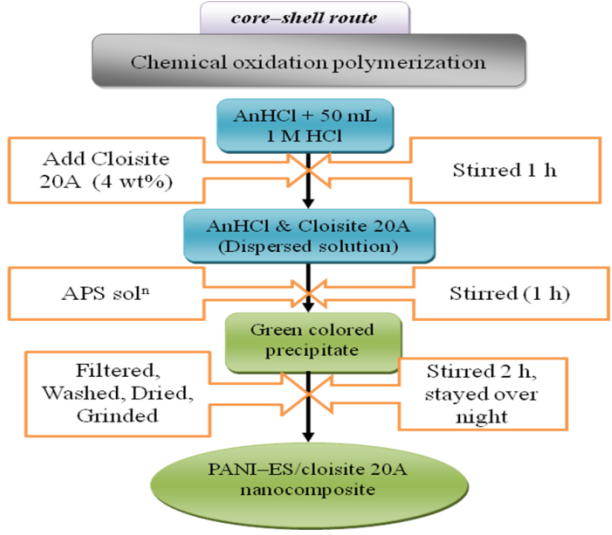

Scheme 3: The Flow Chart for *CORE-SHELL* Route Synthesized PANI-ES/Cloisite 20a (4 Wt%) Nanocomposites

Oxidant solution was added drop wise to the dispersed solution for 1 h and the polymerization was carried out. At that time, the color of the solution changed

from slight blackish to blue and turned into green color and then deep green color. This was observed when the polymerization is continued under constant stirring to 2 h.[22] The obtained dispersion was kept for overnight for complete reaction and polymerization. The resulting dispersion was filtered and washed with 1 (M) HCl, deionized (DI) water, diethyl ether and dried under vacuum at 60 °C for 6 h to get HCl doped PANI-ES/Cloisite 20A nanocomposites. The flow chart for *core-shell* technique synthesis of PANI-ES/Cloisite 20A nanocomposite is shown in **Scheme 3**.

2.4. Pellets Preparation.

Pellets were obtained from as prepared conducting polymeric materials by compression molding using a pelletizer. The assembled plates were first cleaned. A pressure of 124 MPa was applied for five minutes to form pellet. After the removing the pressure, the pelletizer was removed and then the pellet sample was removed. Thicknesses and diameter of prepared pellets were measured to be 1.10 mm and 15.76 mm (pure PANI-ES), 1.09 mm and 15.76 mm (***in situ*** nanocomposite), 1.11 mm and 15.75 mm (***ex situ*** nanocomposite), 1.10 mm and 15.75 mm (***core-shell*** nanocomposite), respectively. These samples were used for characterizations.

2.5. Characterization Techniques.

XRD experiments were performed using a Phillips PW-1710 advance wide angle X-ray diffractometer, Phillips PW-1729 X-ray generator and Cu Kα radiation (wavelength, $\lambda = 0.154$ nm). The generator was operated at 40 kV and 20 mA.

FTIR spectra were recorded on a Thermo Nicolt Nexus 870 spectrophotometer in the range of 400-4000 cm^{-1}. The instrument settings were kept constant (50 scan at 4 cm^{-1} resolution, absorbance mode).

UV-Visible spectra of the pure PANI and its corresponding nanocomposite were recorded by using a Micropack UV-VIS-NIR, DH 2000 in the wave length region 200-1000 cm^{-1}. Base line was corrected before recording the spectra.

Surface morphology of Cloisite 20A, HCl-treated Cloisite 20A, pure PANI-ES, and PANI-ES/Cloisite 20A nanocomposites were analyzed by **SEM** using Carl Zeiss Supra 40 scanning electron microscope. For this experiment, operating voltage was maintained at 30 kV.

To identify the internal structure and dispersion status, the prepared nanocomposite were examined using **HRTEM** at 200 kV acceleration voltages (JEM-2100 HRTEM, JEOL, and Japan). HRTEM experiment specimens of PANI-ES/Cloisite 20A nanocomposites were prepared by microtone technique LEICA Microsystem, GmBH, A-1170) and was transferred them onto Cu TEM grids.

TGA analysis and **DSC** were performed using a Perkin Elmer Pyris Diamond analyzer at a heating rate of 10 °C/min in nitrogen environment.

The room temperature (~30 ^{o}C) **DC conductivity** of the prepared pure PANI-

ES and PANI-ES/Cloisite 20A (4 wt%) nanocomposite was measured using linear four-probe technique. Contact was made with silver paste. A constant current (I) from a current source (Keithley 2400 programmable current source) was allowed to pass through two terminal leads of the four probe and the voltage (*V*) across the other two leads was measured using a multimeter (Keithley 2000 digital multimeter). According to four point-probe method, first the resistivity (ρ) was calculated using the relation[23]

$$\rho = 2\pi S\left(\frac{V}{I}\right) \quad \text{.....} \quad (1)$$

where S is the probe spacing in centimetres (cm), which was kept constant, (I) is the supplied current in millamperes (*mA*) and the corresponding voltage (V) was measured in milivolts (*mV*). The conductivity (σ) was calculated using the relation as follows[23]

$$\sigma = \frac{1}{\rho} \quad \text{.....} \quad (2)$$

Also, resistivity measurement with and without magnetic field as a function of temperature was measured using a linear four-probe technique for understanding of transport phenomenon of prepared pure PANI-ES and PANI-ES/Cloisite 20A (4 wt%) nanocomposite. Resistivity measurement with magnetic field was investigated using a helium compressor (HC) (model HC-4E1)-sumitomo cryostat (model Gains research CO, INC) equipped with 0.8 T superconducting magnet (Lake shore electromagnet). Lake shore 331 temperature controller was used. Such measurements were performed at 5000 gauss and at various temperatures using a computer controlling measuring system. A constant current (*I*) from a current source (Keithley 220 programmable current source) was allowed to pass through two terminals leads of four probe and the voltage (*V*) across the other two leads was measured using a multimeter (2182 NANOVOLTAMETER Keithley).

2.6. Results and Discussion

X−Ray Diffraction (XRD) Study

Low angle (1-10°) X-ray diffraction (LXRD) has often been used to determine the degree of intercalation and/or exfoliation and/or delamination of nanoclays in the polymer matrix. XRD patterns for Cloisite 20A and HCl-treated Cloisite 20A, PANI-ES and PANI-ES/Cloisite 20A (4 wt%) nanocomposites are shown in **Fig. 1**. The different parameters (from XRD analysis) of Cloisite 20A, HCl-treated Cloisite 20A, PANI-ES and PANI-ES/Cloisite 20A (4 wt%) nanocomposites are presented in **Table 1**. The d-spacing in (001) plane has been reported to be 2.42 nm for pure Cloisite 20A nanoclay [21], whereas HCl treated Cloisite 20A clay was

found to be 2.315 nm. This has happened due to the presence of aqueous acidic solution. That plays the role for separation of clay layers [14]. That is why, we got lower d-value. No distinct peak was observed for pure PANI-ES, whereas for *in situ*, *core-shell* and *ex situ* prepared nanocomposites, the small intense peak was found at lower angle. According to [14], it is confirmed that the clay layers were delaminated in the polymer matrix. Acidic aqueous medium has played the major role for delamination along with the interaction between positively charged nitrogen centres in PANI-ES chains and negatively charged centres of oxygen in Cloisite 20A layers ($Si{-}O^{-}$).

Also, the crystallite size (D) of Cloisite 20A, HCl-treated Cloisite 20A, and PANI-ES/Cloisite 20A (4 wt%) nanocomposites (*in situ*, *core-shell* and *ex situ*) was also calculated using the Sherrer's equation 1 [22]

$$D = \frac{0.9\lambda}{\beta \cos\theta} \quad \text{.....(1)}$$

Where D is the crystallite size, λ is wave length of the radiation, θ is the Bragg's angle at (001) reflection and β is the full width at half maxima (FWHM).

In **Fig. 1**, the D-values were found to be 15 nm, 7.88 nm, 9.24 nm and 15.857 nm for PANI-ES, for *in situ*, *core-shell* and *ex situ* prepared nanocomposites, respectively by considering angles between 5 and 45°. FWHM of nanocomposites are significantly lower as compared to pure PANI-ES. Crystallite size and FWHM are inversely related (**Table 1**) [22,23], which has immense impact on property (like crystallinity) enhancement in nanocomposites.

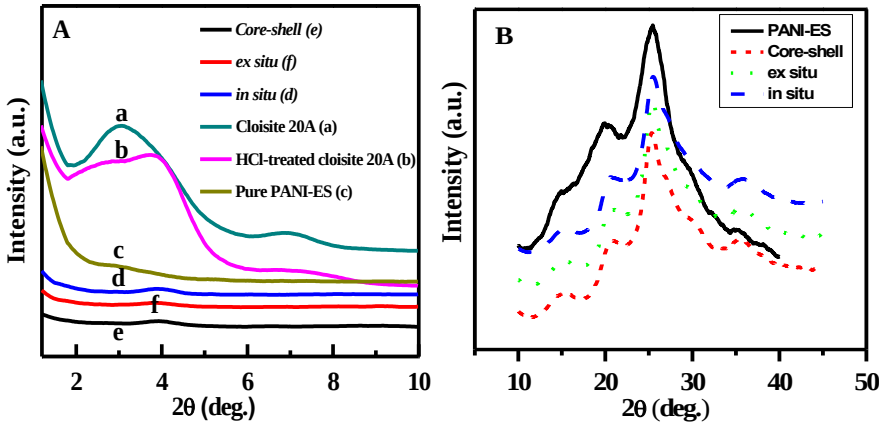

Figure 1. A: Nanostructure study of Cloisite 20A (a), HCl-Cloisite 20A (b), PANI-ES (c), *in situ* nanocomposites (d), *core-shell* nanocomposites (e) and *ex situ* nanocomposite (f); B: Crystallite size study and determination of FWHM of PANI-ES, *in situ* nanocomposites, *ex situ* nanocomposites and *core-shell* nanocomposites

The observed peak positions are found to be at 25.45° for PANI-ES [24],

25.45° for nanocomposite *(in situ*), 25.31° for nanocomposite (*core-shell*) and 25.35° for nanocomposite (*ex situ*). This indicates that the characteristic crystalline phase of the PANI-ES has improved significantly.

Table 1. XRD parameters such as FWHM, crystallite size (D) and nanostructure of Cloisite 20A, HCl-treated Cloisite 20A, PANI-ES, *in situ* nanocomposites, *ex situ* nanocomposites, and *core-shell* nanocomposites

Materials name	**FWHM**	**Crystallite size (D) (nm)**	**Nanostructure**	**Reference no.**
Cloisite 20A	---	---	OMLS	21
HCl treated-cloisite 20A	---	---	Delaminated	14
PANI-ES/20A (*in situ*)	1.008	7.88	Delaminated	14
PANI-ES/20A (*core-shell*)	0.8640	9.24	Delaminated	14
PANI-ES/20A (*ex situ*)	1.1520	15.857	Delaminated	14
PANI-ES	0.582	15	Structure could not assigned	19

Fourier transform infrared (FTIR) spectroscopic analysis

Chemical group analysis of with and without Cloisite 20A, PANI-ES and as prepared nanocomposites (*in situ*, *core-shell* and *ex situ*) was done by FTIR experiment. The presence of chemical groups and shifting of peak positions were observed from FTIR experiment. FTIR spectra of Cloisite 20A [23], HCl-treated Cloisite 20A, PANI-ES [24] and PANI-ES/Cloisite 20A nanocomposites (*in situ, core-shell* and *ex situ*) are shown in the **Fig. 2**. The characteristic peak positions and peak assignments are given in the **Table 2**. In Fig. 3.2, the most important Si−O stretching of Cloisite 20A and HCl-treated Cloisite 20A was found to be at 1040 cm^{-1} [16]. However, there are some extra bands found in Cloisite 20A, whereas these bands are not exhibited in MMT clay. These bands are located at 2924, 2842 and 1475 cm^{-1} and are assigned for C−H symmetric, asymmetric and bending vibrations of methylene groups, respectively. Similarly for HCl-treated Cloisite 20A, Si−O band position is not changed (it is also clearly evident from SEM images in **Fig. 4**). FTIR spectra of

PANI-ES [20] and PANI-ES/Cloisite 20A (4 wt%) nanocomposites (*in situ, core-shell* and *ex situ)* are shown in **Fig. 2**. The important FTIR bands of PANI-ES were found at 1554, 1475 and 1108 cm^{-1} corresponding to quinoid, benzenoid and C=N stretching, respectively [16]. From this observation, the presence of quinoid and benzenoid ring vibrations (at 1475 and 1554 cm^{-1}) indicates the oxidation state of PANI-ES [20].

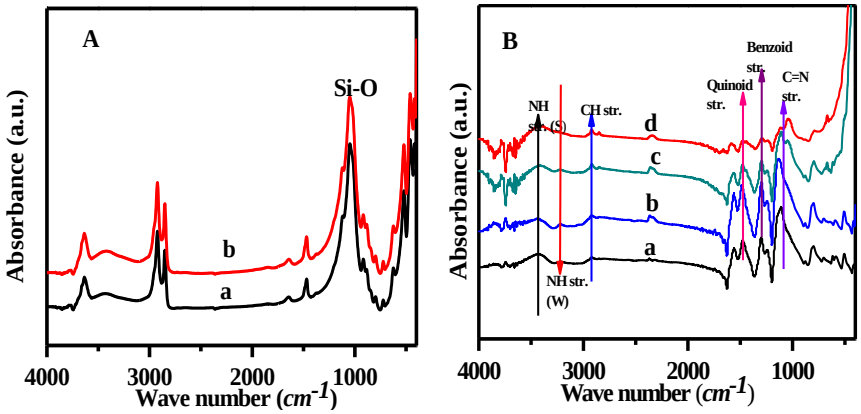

Figure 2. A: FTIR spectra of Cloisite 20A (a) and HCl-treated Cloisite 20A (b); B: PANI-ES, *in situ* nanocomposites, *ex situ* nanocomposites and *core-shell* nanocomposites

The characteristic bands of *in situ* nanocomposites were observed at 1556, 1473, 3441and 1132 cm^{-1} (**Fig. 2**). These bands are shifted towards higher wave number which indicates the interaction occurring between PANI-ES chains and Cloisite 20A. For *ex situ* nanocomposites (**Fig. 2**), the bands have appeared at 3425, 1567, 1460, and 1107 cm^{-1}. The FTIR bands of *core-shell* nanocomposites are found at 3432, 2926, 1588, 1474, and 1034 cm^{-1} (**Fig. 2**). The C=N bands of prepared PANI-ES/Cloisite 20A (4 wt%) nanocomposites *(in situ)*, *core-shell* nanocomposites and *ex situ* nanocomposites were found to be at 1132 cm^{-1}, 1034 cm^{-1} and 1107 cm^{-1}, respectively. It was described as the "electron−like–band". This was considered to be the delocalization of electrons in the polymer chain. The stretching vibrations of the $C-N^{\cdot+}$ in the polaron structure of PANI-ES, *in situ* and *ex situ* nanocomposites were found to be at 1236, 1247 and 1244 cm^{-1}, respectively. The peak positions in benzenoid ring of PANI-ES and its corresponding *in situ*, *core-shell* and *ex situ* nanocomposites were observed at 1473, 1479, 1474 and 1489 cm^{-1}, respectively. Similarly, the stretching vibrations of C=C in the quinoid ring of PANI-ES, *in situ* nanocomposites, *core-shell* nanocomposites and *ex situ* nanocomposites were found to be at 1556 cm^{-1}, 1560 cm^{-1}, 1588 cm^{-1} and 1560 cm^{-1}, respectively. This indicates that the characteristic peaks of PANI-ES chains are shifted to higher wave numbers due to the strong interaction between HCl doped PANI-ES and negatively charged species of used clay platelet [16]. It is well known that the strong interaction between the clay platelet and PANI-ES would facilitate a charge transfer process between the components of the system, which further contributes to the increment of the conductivity of the nanocomposites. Also, this result is clear evidence of the presence

of different chemical groups in Cloisite 20A and PANI-ES chains.

Table 2. FTIR Peak positions and peak assignments of Cloisite 20A, HCl-treated Cloisite 20A, PANI-ES, *in situ* nanocomposites, *ex situ* nanocomposites, and *core-shell* nanocomposites

Peak Assignments	**Peak Positions (cm^{-1})**					
	Cloisite 20A	**HCl treated Cloisite 20A**	**PANI-ES**	**PANI-ES/20A (*in situ*)**	**PANI-ES/20A (*core-shell*)**	**PANI-ES/ 20A(*ex situ*)**
N−H stretch (weak)	N[a]	N[a]	3217	3220	N[a]	3220
N−H stretch (strong)	N[a]	N[a]	3419	3441	3432	3425
C−H stretch	N[a]	N[a]	2926	2926	2926	2926
Quinoid stretch	N[a]	N[a]	1554	1556	1588	1567
Benzoid stretch	N[a]	N[a]	1475	1473	1474	1460
C=N stretch	N[a]	N[a]	1108	1132	1034	1107
Si−O stretch	1055	1055	N[a]	N[a]	N[a]	N[a]
Reference	16	N[a]	20	N[a]	N[a]	N[a]

[a]N stands for no peak

UV-visible (UV-Vis) spectroscopic analysis

Dispersed solution of Cloisite 20A and HCl-treated Cloisite 20A exhibits an absorbing peak at 262 nm, due to the scattering and/or absorption from the clay layers with lateral sizes from 50 to 200 nm [25]. The small band appears at 305 nm for Cloisite 20A and HCl-treated Cloisite 20A due to the presence of organic modified group in Cloisite 20A clays. Also, it is clear from **Fig. 3** and **Table 3** that PANI-ES shows characteristic peaks at 312 and 346 nm correspond to π-π^* transition of the benzenoid ring and 618 nm peak for electronic excitation from benzenoid ring to quinoid ring [16].

UV-Vis spectra of prepared nanocomposites exhibited two characteristic bands similar to the PANI-ES. Peaks were observed at 336 and 635 nm for nanocomposites prepared *via in situ* method, 303 and 588 nm for nanocomposites prepared *via core-shell* route *and* 349 and 633 nm for nanocomposites prepared *via ex situ* technique.

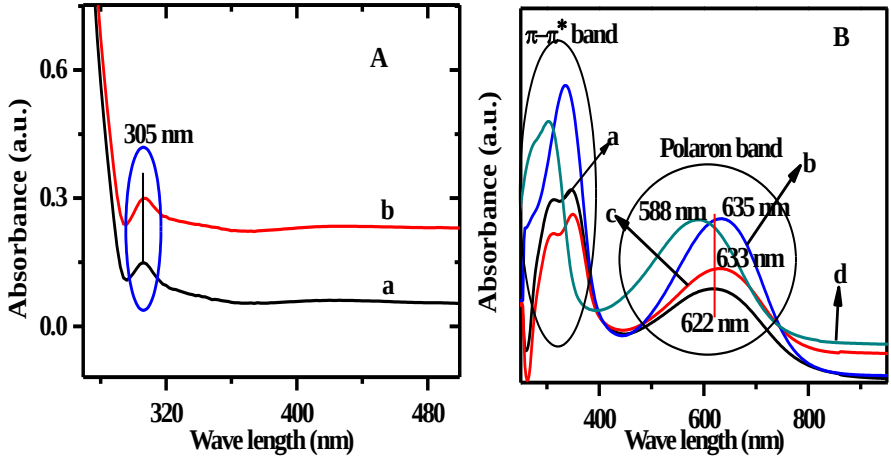

Figure 3. A: UV-Vis spectra of Cloisite 20A (a) and HCl-treated Cloisite 20A (b); B: PANI-ES (a), *in situ* nanocomposite (b), *ex situ* nanocomposite (c) and *core-shell* nanocomposites (d)

Table 3. UV-Vis peak positions and peak assignment of Cloisite 20A, HCl-treated Cloisite 20A, PANI-ES, *in situ* nanocomposites, *ex situ* nanocomposites, and *core-shell* nanocomposites

Materials name	**Figure(s)**	**Peak Positions (nm)**	**Peak Assignments**
Neat Cloisite 20A	3.3A	262 & 305	Scattering of clay platelet & organic modified group
HCl-treated Cloisite 20A		262 & 305	Scattering of clay platelet & organic modified group
PANI-ES	3.3B	327−316 & 618	π-π^* transition & π-polaron transition
***in situ* nanocomposites**		336 & 635	π-π^* transition & π-polaron transition
***ex situ* nanocomposites**		308-349 & 633	π-π^* transition & π-polaron transition
***core-shell* nanocomposites**		303 & 588	π-π^* transition & π-polaron transition

Scanning electron microscopy (SEM)

SEM images with magnification 20 kX for Cloisite 20A, HCl-treated Cloisite 20A, PANI-ES, and PANI-ES/Cloisite 20A (4 wt%) nanocomposites (*in situ, core-shell* and *ex situ*) are shown in **Fig. 4.** As evident from SEM images, Cloisite 20A and HCl-treated Cloisite 20A possess similar type of morphology and it is crystal-like (**Fig. 4A and 3.4B**). SEM image of HCl doped PANI-ES is shown **Fig. 4C** which possesses tangled fiber-like morphology. SEM images of PANI-ES/Cloisite 20A (4 wt%) nanocomposites (*in situ, core-shell* and *ex situ*) are also shown in **Fig 4D, 4E** and **4F**, respectively) which possess aggregated tangled fiber-like images. These results showed clearly that Cloisite 20A participate in the closering of the PANI-ES Chains. Hence, these nanocomposites become more ordered state. Generally, ordered materials showed better electrical conductivity. The diameters of these compacted tangled fibers were found to nano regime dimension, which is providing higher surface area. Particularly for gas sensor application, it may be helpful to diffuse more gas molecules and show better response.

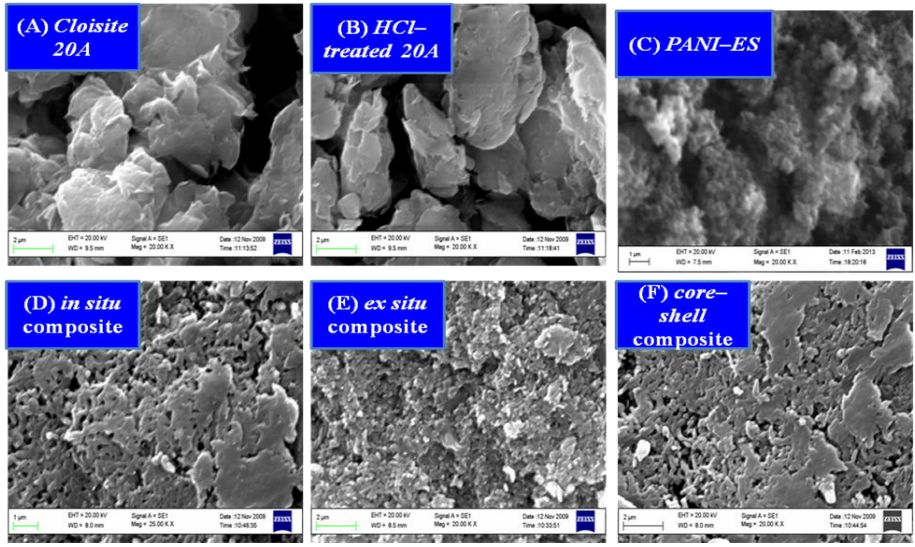

Figure 4. SEM images of Cloisite 20A (A), HCl-treated Cloisite 20A (B), PANI-ES (C), *in situ* nanocomposites (D), *ex situ* nanocomposites (E) and *core-shell* nanocomposites (F)

High resolution transmission electron microscopy (HRTEM)

The morphology of the resulting nanocomposites was observed using high resolution transmission electron microscopy (HRTEM). **Fig. 5** showed the typical HRTEM images of the PANI-ES/Cloisite 20A nanocomposites (*in situ, core-shell* and *ex situ*). HRTEM image in **Fig. 5A** showed a distribution of Cloisite 20A in *in situ* nanocomposite. For this nanocomposite, disorder layers in the nanoregime were found in **Fig. 5D**. This indicates that Cloisite 20A layers were delaminated. This result

is supported by XRD analysis. Similar results were found in other two prepared nanocomposites. But the main difference is dispersion and disorder criteria. HRTEM images are shown in **Fig. 5B, 5C, 5D, 5E**, **5F**. It was observed that the whole Cloisite 20A particles were covered by uniform PANI-ES Chains, which indicated the formation of apparent *core-shell* structures. This result showed a well dispersion in PANI-ES matrix.

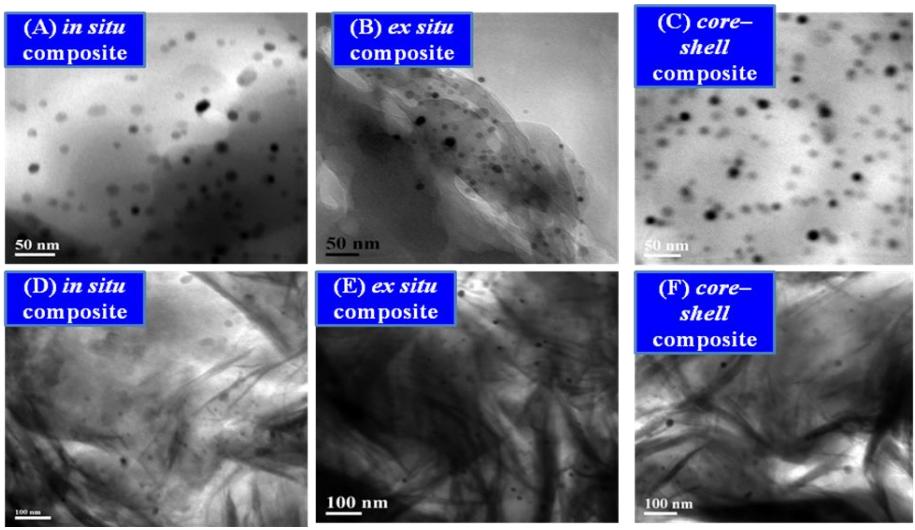

Figure 5. HRTEM image of (A) *in situ* nanocomposites, (B) *ex situ* nanocomposites, (C) *core-shell* nanocomposites for study of dispersion of Cloisite 20A and (D) *in situ* nanocomposites, (E) *ex situ* nanocomposites and (F) *core-shell* nanocomposites for study of disordered structure

DC conductivity measurements

At room temperature, DC conductivity of the PANI-ES and PANI-ES/Cloisite 20A nanocomposites (*in situ, core-shell* and *ex situ*) were measured using linear four-probe technique. For this measurement, pellet samples were used. The average DC conductivity values of PANI-ES and as prepared nanocomposites are presented in **Table 4**. The DC conductivity of PANI-ES was found to be 1.92 S/cm. With the addition of 4 wt% Cloisite 20A nanoclays, the conductivity of prepared PANI-ES is increased. The conductivity of as prepared nanocomposites (*in situ, core-shell and ex situ*) was found to be 3.87, 5.12 and 2.75 S/cm, respectively. $I-V$ Characteristics of PANI-ES and PANI-ES/Cloisite 20A (4 wt%) nanocomposites (*in situ, core-shell and ex situ*) are shown in **Fig. 6**. It is seen from **Fig. 6** that the applied current(s) and obtained voltage(s) are linearly related, showing ohmic behaviour [28].

The higher compacted PANI-ES chains in PANI-ES/Cloisite 20A (4 wt%) nanocomposites (*in situ, core-shell* and *ex situ*) leads more localized site (π-bond to the exciton band) and hence, higher amount of charge carrier occurs.

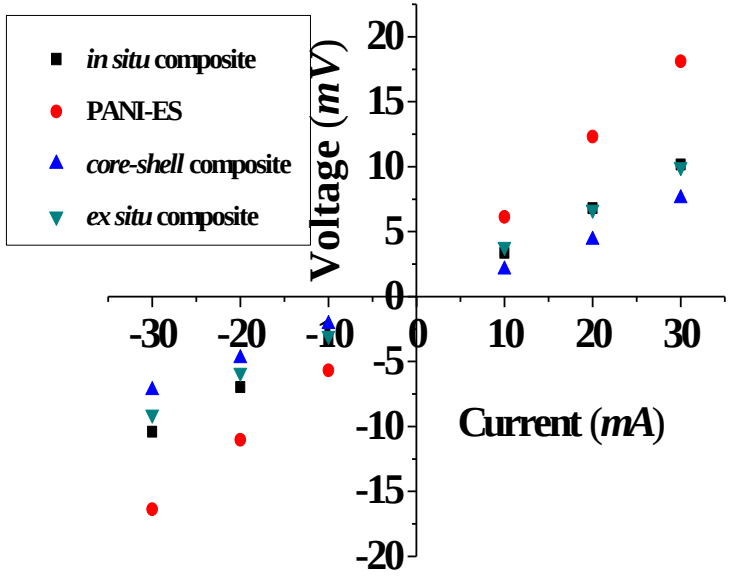

Figure 6. Room temperature *I−V* characteristics of PANI-ES, *in situ* nanocomposites, *ex situ* nanocomposites and *core-shell* nanocomposites

This indicates the higher carrier path and shows the higher DC conductivity of as prepared nanocomposites than HCl doped PANI-ES. This is really an interesting observation. In *core-shell* structure nanocomposite, the compactness is more than other prepared nanocomposites. That means Cloisite 20A connects more the PANI-ES Chains which increase the carrier paths. Therefore, it gives more DC conductivity [27,28].

Table 4. Room temperature DC conductivity of PANI-ES/MMT, PANI-ES/15A, PANI-ES, *in situ* nanocomposites, *ex situ* nanocomposites, and *core-shell* nanocomposites

Materials Name	**PANI-ES /MMT**	**PANI-ES /15A**	**PANI-ES**	**PANI-ES/20A (*in situ*)**	**PANI-ES/20A (*core-shell*)**	**PANI-ES/20A (*ex situ*)**
σ (S/cm)	1.20	1.650	1.92	3.87	5.12	2.75

The variation of DC conductivity with temperature is shown in **Fig. 7**. It was observed that PANI-ES and prepared nanocomposites showed increase of conductivity with the increase of temperature from 50 to 300 K. This behaviour is similar to the behaviour of inorganic semiconductor. Hence it can be called as organic semiconductor [29,30].

Various models were used to find the probable transport mechanism of conducting polymers which requires below room temperature. DC conductivity was

measured in a temperature range 77-300 K in the present work and fitted the Mott's variable range hoping (Mott's VRH) model and Arrhenius model to analyse the transport mechanism. According to Mott's VRH model, the temperature (T) dependence DC conductivity follows the expression [29,30]

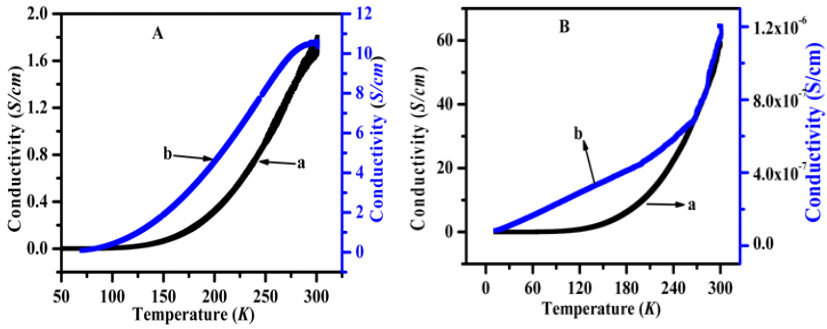

Figure 7. A: Temperature dependent DC conductivity of PANI-ES (a) and *in situ* nanocomposites (b); B: *core-shell* nanocomposites (a) and *ex situ* nanocomposites (b)

$$\sigma = \sigma_0 \exp\left(-\frac{T_0}{T}\right)^r \text{.....(2)}$$

Where T_0 is the Mott characteristic temperature and σ_0 the limiting value of conductivity at infinite temperature and the exponent 'r' is related to the dimensionality of the transport process via the expression r = [1/(1+d)], where d=1, 2 and 3 for one, two and three dimensional conduction process, respectively. The Mott's 3D VRH plots are presented in **Fig. 8** (**A** and **B**).

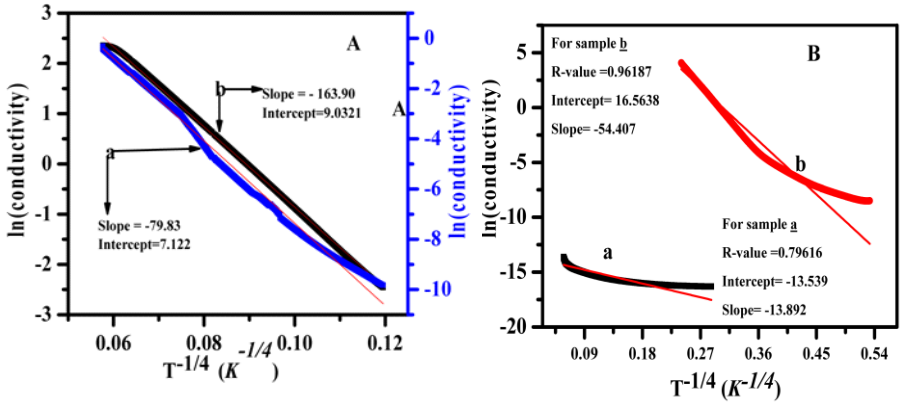

Figure 8. A: Logarithmic variation of DC conductivity of PANI-ES (a) and *in situ* nanocomposites (b); B: *core-shell* nanocomposites (a) and *ex situ* nanocomposites (b)

As another possibility, it may satisfy the Arrhenius model and this was used to measure the activation energy. **Fig. 9** shows the Arrhenius plot of measured DC conductivity as a function of reciprocal temperature. In Arrhenius model, the temperature dependent DC conductivity follows [29,30] the equation (3)

$$\sigma = \sigma_0 \exp\left(-\frac{E_a}{kT}\right) \text{.....(3)}$$

Where E_a is the thermal activation energy of the electrical conduction and σ_a is a parameter depending on the semiconducting nature. The better linear dependency, *i.e.*, regression value (after linear fit) of conductivity *vs* temperature (Mott's VRH model and Arrhenius model) follows that the transport process corresponds either Mott's VRH model or Arrhenius model [30-32]. The regression values (both Mott's VRH model and Arrhenius model) are presented in **Table 5**. Accordingly, the better regression value was found in Mott's 3D-VRH model (0.99856 for PANI-ES and 0.99098 for *in situ* nanocomposite, 0.96187 for *core-shell* nanocomposite and 0.79616 for *ex situ* nanocomposite). Hence, it follows the Mott's 3D-VRH model which is consistent with the results reported in the literature [30-32]. This suggests that charge carrier can hop both in between the chains, *i.e.,* interchain hopping and along the chain, *i.e.,* intrachain hopping as PANI-ES has chain structure [30-32].

Table 5. Regression value (R-value) of PANI-ES, in situ nanocomposites, ex situ nanocomposites and core-shell nanocomposites from linearly fitted data (3D-VRH and Arrhenius model)

R-values	**PANI-ES**	***in situ* nanocomposite**	***core-shell* nanocomposite**	***ex situ* nanocomposite**
3D-VRH	0.99856	0.9984	0.96187	0.79616
Arrhenius model	0.97381	0.97026	0.75038	0.61723

According to 3D-VRH model, the temperature dependence of DC conductivity can be presented in equation (4) as follows [30-34]

$$\sigma = \sigma_0 \exp\left(-\frac{T_0}{T}\right)^{\frac{1}{4}} \text{.....(4)}$$

T_0 and σ_0 were also calculated from VRH plot $\ln\sigma$ vs $T^{-1/4}$ of prepared nanocomposites along with PANI-ES and is presented in **Table 3.6**. All nanocomposites show higher localization length (nanometer) than pure PANI-ES. This effect may be due to the presence of nanoclays in the PANI-ES chains [18]. These are partially block the conductive path [18]. Therefore, charge carriers could not hop easily from one chain to another chain. On the other hand, the clay based nanocomposites prepared by *core-shell* route indicates higher localization length than

other prepared nanocomposites. This has happened due to the presence of more clay particles in the PANI-ES chains and which affect the localisation length (L_{loc}).

We analyzed the resistivity data by the 3D-VRH model among localized states as described in the literature [32,33]

$$\rho(T) = \rho_0 \, e^{\left(\frac{T_{Mott}}{T}\right)^{\frac{1}{4}}} \quad \text{.....(5)}$$

$$T_{Mott} = \frac{16}{\left[K_B N(E)_F L^3_{loc}\right]} \quad \text{.....(6)}$$

Where K_B is the Boltzmann constant; $N(E)_F$ is the density of states at the Fermi level; and L^3_{loc}; the localization length. We plotted lnσ *vs* $T^{-1/4}$. This plot exhibits a straight line after linear fit for all prepared materials as shown in **Fig. 8**. T_{Mott} can be evaluated from slope of the straight line and listed in **Table 6**. The localization length L_{loc} can be calculated from temperature dependent conductivity at particular magnetic field (0.5 T) data as shown in **Fig. 10**. From the Mott expression, the resistivity at different temperatures at a particular magnetic field can be written as [30-32]

$$\ln\left[\frac{\rho(H)}{\rho_0}\right] = t\left(L_{loc} / L_H\right)^4 \left(\frac{T_{Mott}}{T}\right)^{\frac{3}{4}} \quad \text{.....(7)}$$

Where, t = 5/2016, $L_H = (hc/2\pi eH)^{1/2}$ = magnetic length, c = velocity of light (3×10^{10} cm/s), h = Planck's constant (6.62×10^{-27} erg.sec), e = electronic charge (1.6×10^{-19} C) and H = 0.5 tesla (T) is the applied magnetic field. **Fig. 10** shows the plot of ln [ρ (H, T)/ρ(0)] against $T^{-3/4}$, which is a straight line for each sample. From the slope, we determined the values of L_{loc} and are listed in **Table 6**. Using the values of T_{Mott} and L_{loc} for each sample in equation (6), the values of $N(E)_F$ was calculated and are presented in **Table 6**.

$$R_{hop,Mott} = \left(\frac{3}{8}\right)\left(\frac{T_{Mott}}{T}\right)^{\frac{1}{4}} L_{loc} \quad \text{.....(8)}$$

$$\Delta_{hop,Mott} = \left(\frac{1}{4}\right)\left(k_B T\right)\left(\frac{T_{Mott}}{T}\right)^{\frac{1}{4}} \quad \text{.....(9)}$$

Using the values of $T_{0,Mott}$, L_{loc} and $N(E_F)$, we calculated the mean hopping distance ($R_{hop,Mott}$) and the energy difference between sites ($\Delta_{hop,Mott}$) from the equation 8 and 9 and the data are presented in **Table 3.6** [30-32].

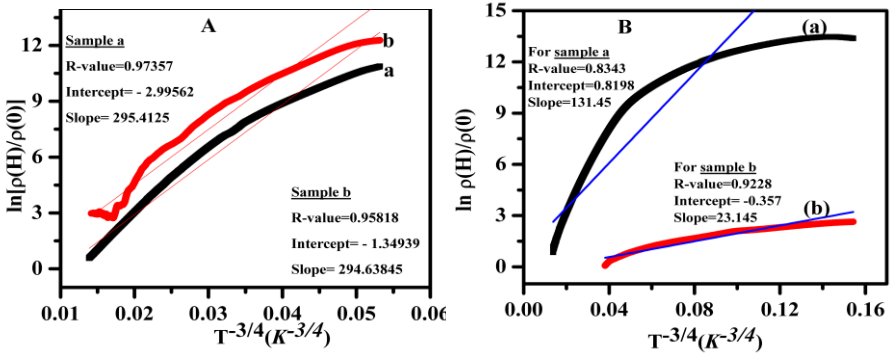

Figure 10. A: Plots of [ln ρ(H)/ρ(0)] *vs* $T^{-4/3}$ for PANI-ES (a) and *in situ* nanocomposite (b) at 0.5 T; B: Plots of [ln ρ(H)/ρ(0)] *vs* $T^{-4/3}$ for *core-shell* nanocomposite (a) and *ex situ* nanocomposite (b) at 0.5 T

Table 6. Conduction parameters obtained by analysing low temperature resistivity/conductivity with and without field data of PANI-ES, in situ nanocomposites, ex situ nanocomposites and core-shell nanocomposites

Conducting parameters	**PANI-ES**	***in situ* nanocomposite**	***core-shell* nanocomposite**	***ex situ* nanocomposite**
Slope (without field)	-80.6126	-79.83	-54.4071	-13.5396
Intercept (without field)	22.4947	7.1224	16.538	13.892
Slope (with field)	295.4125	294.6384	131.4528	23.1452
σ_0	5.87×10^9	1.239×10^3	1.56×10^7	1.079×10^6
T_{Mott} **(*K*)**	4.22×10^7	4.0613×10^7	8.7×10^6	3.355×10^4
L_{loc} **(*nm*)**	274.68	277.18	301.24	549.28
N (E_F) (no. states/*eV*/*cm*^{3})	2.12×10^{19}	2.15×10^{17}	7.8×10^{17}	3.33×10^{19}
Temperature (*K*) at M-I transition	100	104	90	100
$R_{hop,\ Mott}$ **(°*A*)**	262.5	259.8	199.2	88.15
$\Delta_{hop,\ Mott}$ **(m*eV*) at M-I transition)**	54.9	56.01	34.19	9.22
k (*eV*/*K*)	8.62×10^{-5}	8.62×10^{-5}	8.62×10^{-5}	8.62×10^{-5}

Using the parameters in the above expression, the values of $R_{hop,Mott}$ and $\Delta_{hop,Mott}$ were calculated at metal-insulator (M-I) transition point. At particular temperature, this transition is possible. The temperature is estimated at M-I transistion and is presented in **Table 6**. In addition, the obtained hopping parameters helped to understand the 3D-VRH mechanism of as prepared materials.

Thermogravimetric (TG) analysis

Fig. 11 shows the typical TGA curves of Cloisite 20A, HCl-treated Cloisite 20A, HCl doped PANI-ES and PANI-ES/Cloisite 20A (4 wt%) nanocomposites (*in situ*, *core-shell* and *ex situ*), as measured under a nitrogen (N_2) atmosphere. From the above TGA curves, it is seen that the HCl doped PANI-ES starts degradation at 110 ºC (12% weight loss), but the nanocomposites degrades at 128 ºC (6% weight loss) for loading of 4 wt% Cloisite 20A nanoclays. The residual weight was also found to be higher than that of pure PANI-ES. This certainly indicates the release of bound water molecule from PANI-ES and its corresponding nanocomposites. The moisture content of 4 wt% PANI-ES/Cloisite 20A nanocomposites (*in situ*, *core-shell* and *ex situ*) is less due to the presence of Cloisite 20A, *i.e.*, hydrophobicity of PANI-ES increases. This was followed by rapid weight loss (up to 500 ºC) of neat PANI-ES and as prepared nanocomposites (*in situ*, *core-shell* and *ex situ*). This is due to the release of HCl molecule (up to 500 ºC) when the third stage degradation started. Final stage degradation occurred for neat PANI-ES and nanocomposites prepared by *in situ*, *core-shell* and *ex situ* method to complete degradation and decomposition of PANI-ES backbone. TGA curves clearly indicate that prepared nanocomposites are thermally stable than HCl doped PANI-ES due to the presence of Cloisite 20A nanoclays. Here, the Cloisite 20A platelets act as barriers to heat flow due to their high aspect ratio and hindered the degradation process [28].

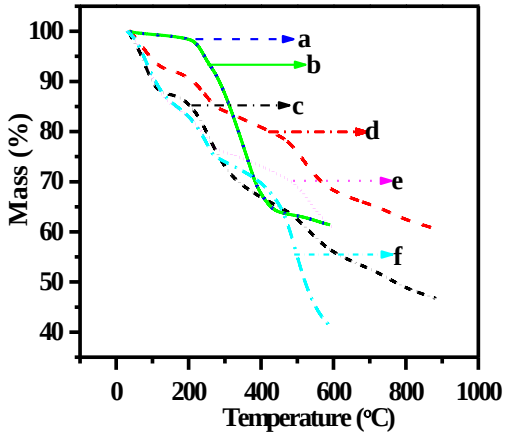

Figure 11. TGA plots of Cloisite 20A (a), HCl-treated Cloisite 20A (b), pure PANI-ES (c), *in situ* nanocomposites (d), *ex situ* nanocomposites (e), and c*ore-shell* nanocomposites (f)

Differential scanning calorimetric (DSC) analysis

The crystallinity of polymer is typically calculated by DSC analysis and equation 10 as follows [33,34]

$$\%\,\text{Crystallinity} = \frac{\Delta H^{m}}{\Delta H^{m}{}_{0}} \times 100 \quad \text{.....(10)}$$

Where ΔH^m is the enthalpy of fusion of the polymer samples which is determined by area of the peak at melting temperature and $\Delta H^m{}_0$ is enthalpy of fusion of the totally crystalline polymer measured at equilibrium melting temperature in degree centigrade (°C). The enthalpy of fusion is estimated are 447.097 for PANI-ES, 324.25 for *in situ*, 859.296 for *core-shell* and 227.19 for *ex situ* nanocomposites, respectively. The neat PANI-ES as well as PANI-ES/Cloisite 20A nanocomposites (*in situ, core-shell* and *ex situ*) is presented in **Fig. 12**. According to the equation 10, % crystallinity is directly related to the ΔH^m. Higher the enthalpy of fusion at melting temperature more be the crystallinity. Hence, % crystallinity of PANI-ES/Cloisite 20A (4 wt%) nanocomposites (*in situ, core-shell* and *ex situ*) shows higher crystallinity than pure PANI-ES. Since Cloisite 20A can be attributed in closer chain arrangements and hence, increases the compactness, *i.e.*, more is the crystallinity [33,34].

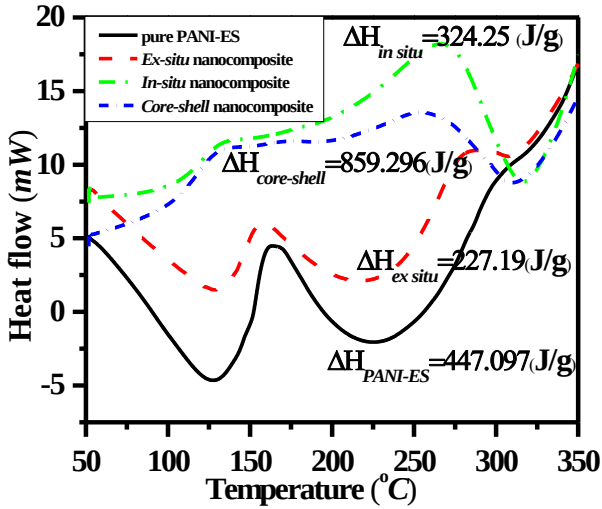

Figure 12. DSC thermograms of PANI-ES, *in situ* nanocomposites, *core-shell* nanocomposites and *ex situ* nanocomposites

2.4. Response Of Nitrogen Dioxide (I.E., No_2 Gas Sensor)

Nitrogen dioxide (NO_2) is one of the important compositions of vehicle exhaust, emissions of the thermal power plant, and chemical production industries [35, 36]. The main sources of NO_2 are acid rain and photochemical smog. It is very harmful

to the plant, structural components, and equipments [37, 38]. NO_2 is a colorless, flammable, and dangerous gas even at very low concentration. It is a reddish-brown color gas at high temperature. Additionally, the reaction between NO_2 and CO in the presence of sunlight is to produce ozone (O_3). Ozone acts as a oxidizing agent and is believed to be harmful to plants and the respiratory system of human beings and animals. Due to the toxic nature of NO_2 gas, it causes some serious problems of human being *i.e.*, heart failure, arrhythmia and other cardiovascular. if the humans inhaled in large amounts, it may cause death [39]. Hence, from the protection of public health and environmental, the detection of nitrogen dioxide is great scientific challenge. Implication of monitoring and measuring system for NO_2 gas, it has great support to decrease the damage level and keep humane heath safe. So far, scientific community have been put there lots of efforts for developing a variety of NO_2 gas sensor systems (such as semiconductor sensor [40], capacitive type sensor [41], and Surface acoustic wave (SAW) sensor [42]). Till to discovery of conducting polymers, the metal oxides based films have been used extensively for detecting the gas. The sensors have lack high sensitivity and have operated at high temperature (300–500 ◦C) [43, 44].

The conducting polymers have many potential applications for making different devices with their combined properties such as optical, electrochemical, and electrical properties [45]. In the conducting polymer family, polyaniline (PANI) is one of the member and has received attention widespread. This is due to mechanical flexibility, high environmental stability, ease of processing, simple and reversible doping/dedoping chemistry, and modifiable electrical conductivity [46-49].

Polyaniline based gas sensors have been taking significant consideration in last few decades [50, 51]. It has unique electrical conductivity. PANI has ability to transport charge carriers in both ways *i.e.*, inter polymer chain and intra polymer chains. Therefore, polyaniline can willingly react with reductive and oxidative agents, to change their electrical performance at room temperature.

Nanostructured polyanilines *i.e.*, nanowires, nanofibers, and nanorods, have been shown better performance due to their high aspect ratio's. This helps the fast diffusion of gas molecules into the structures. Some reports are available for synthesizing of polyaniline nanofiber [52-54]. The diameter of polyaniline nanofibers are obtained with nearly uniform diameters between 30 and 120 nm.

There are different forms of polyaniline. Emeraldine salt form (half-oxidization and half-de oxidization state) of polyaniline has the highest conductivity in the PANI family. The conductivity of polyaniline decreases with increase the extent of oxidization [55]. Particularly, NO_2 gas (oxidizing character) was exposed on polyaniline, the degree of oxidization of polyaniline would increase. Consequently, its conductivity decreases. Therefore, the experimental results are shown in Figure 13. It can be explained by the extent of oxidation state of polyamine. When exposed NO_2 gas on polyaniline, the conductivity decreases. This is due to increase the extent of oxidation. Brief summary of NO_2 detection is presented in Table 7.

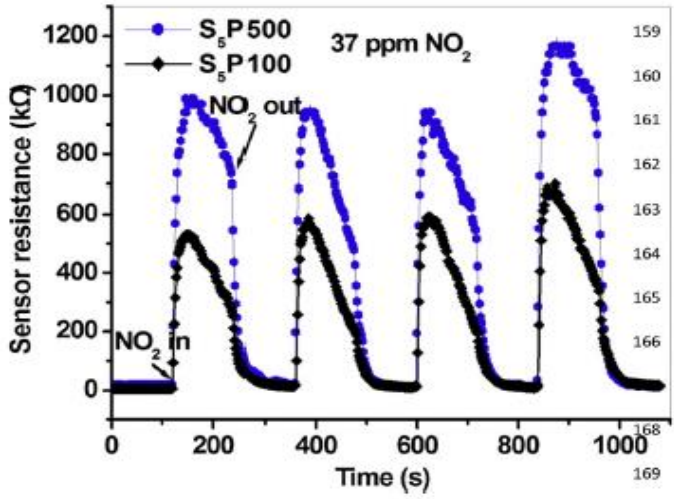

Figure 13. [56] The response nitrogen dioxide (NO_2) of PANI-ES based sensor measured at 37 ppm NO_2 gas concentrations at ambient condition-

Table 7. Brief summary of NO_2 detection

Study	Materials	Perporfamce	Optimum temperature (^{0}C)	Limitation
Yan et al. [57]	polyaniline nanofibers	Response time xxx s	Room Temperature	Medium NO2 concentration
Kim et al. [58]	An organic conductive nanocomposite	Sensitivity xxx %	Room Temperature	High NO2 concentration
Kumar et al. [59]	Plasma Polymerized Nanostructure Polyaniline **Thin Film**	Response time xxxx s	Room Temperature	Medium NO2 concentration
Surwade et al. [60]	poly-o-toluidine	Response time 5 s	Room Temperature	Low-Medium NO2 concentration
Xie et al. [61]	Polyaniline based ultra-thin film	Response time xxx s	Room Temperature	Low NO2 concentration
Rozemarie et al. [62]	Polyaniline based electrospun	Sensitivity 45 %	Room Temperature	High NO2 concentration
Haynes et al. [63]	Polyaniline		Room Temperature	High NO2 concentration

2.5. Conclusions

We have successfully prepared PANI-ES/Cloisite 20A nanocomposites in *in situ, core-shell* and *ex situ* polymerization routes. The silicate layers of the clay platelets were delaminated after addition of Cloisite 20A in aqueous HCl medium during the synthesis of PANI-ES and nanocomposites. The PANI-ES/Cloisite 20A nanocomposites (*in situ, core-shell and ex situ*) exhibited remarkable improvement of DC electrical conductivity, thermal stability and enthalpy of fusion compared to pure PANI-ES. We described the concurrent improvement the properties like electrical DC conductivity, thermal stability and enthalpy of fusion of the prepared nanocomposites. Temperature dependent DC conductivity of prepared nanocomposite samples was observed. The linear fit data favoured to the Mott's 3D−VRH mechanism. The resistivity with magnetic field 0.5 T of HCl doped PANI-ES, PANI-ES/Cloisite 20A (4 wt%) nanocomposites (*in situ, core-shell* and *ex situ* polymerization route*)* were performed in the range of 77−300 K to estimate the L_{loc} of 274.68 nm, 277.18 nm, 301.24 nm and 549.28 nm for HCl doped PANI-ES and PANI-ES/Cloisite 20A (4 wt%) nanocomposites (*in situ, core-shell* and *ex situ* polymerization route*)*, respectively. The resistivity at 0.5 T of prepared materials follows the Mott's expression. Varieties of physical parameters such as $N(E_F), T_{Mott}, L_{loc}, R_{hop}, and\ \Delta_{hop}$ corresponds to transport mechanism are estimated in the presence and absence of magnetic field. The nitrogen dioxide gas responses and mechanism of polyaniline based materials were studied in details.

3.0. Acknowledgments

The author conveys their sincere thanks to the CRF, IIT Kharagpur for their providing testing facilities and Materials Science Centre to do the research work. I would like to thank Prof. Debabrat Pradhan for their invaluable guidance, advices, constant inspiration and technical support throughout the entire research program.

4.0. References

[1] Saini, P., Choudhary, V., Vijayan, N., and Kotnala, R. K. 2012, Improved Electromagnetic Interference Shielding Response of Poly(aniline)-Coated Fabrics Containing Dielectric and Magnetic Nanoparticles, Journal of Physical Chemistry C, Vol. 116, pp. 13403-13412.

[2] Burroughes, J. H., Bradley, D. D. C., Brownn, A. R., Marks, R. N., Mackay, K., Friend, R. H., Burns, P. L., and Homes, A. B. 1990, Light-emitting Diodes Based on Conjugated Polymers, Nature, Vol. 347, pp. 539-541**.**

[3] Frackowiak, E., Khomenko, V., Jurewicz, K., Lota, K., and Be'guin F. 2006, Supercapacitors Based on Conducting Polymers/Nanotubes Composites, Journal of Power Sources, Vol. 153, pp. 413-418.

[4] Wu, F., Chen, J., Chen, R., Wu, S., Li, L., Chen, S., and Zhao, T. 2011,

Sulfur/Polythiophene with a Core/Shell Structure: Synthesis and Electrochemical Properties of the Cathode for Rechargeable Lithium Batteries, Journal of Physical Chemistry C, Vol. 115, pp. 6057-6063.

[5] Yu, L., Jin, X., and Zeng, X. 2008, Methane Interactions with Polyaniline/ Butylmethylimidazolium Camphorsulphonate Ionic Liquid Composite, Langmuir, Vol. 24, pp. 11631-11636.

[6] Racicot, R., Richard Brown, R., and Yang, S. C. 1997**,** Corrosion Protection of Aluminium Alloys by Double-strand Polyaniline, Synthetic Metals, Vol. 85, pp. 1263-1264.

[7] MacDiarmid, A. G., Chang, J. C., Richter, A. F., and Epstein, A. J. 1987, Polyaniline: A New Concept in Conducting Polymers, Synthetic Metals, Vol. 18, pp. 285-290.

[8] Yue, J., Epstein, A. J., Zhong, Z., Gallagher, P. K., and MacDiarmid, A. G. 1991 Thermal Stabilities of Polyaniline, Synthetic Metals, Vol. 41, pp. 765-768.

[9] Cao, Y., Smith, P., and Heeger, A. J. 1992, Counter-ion Induced Processability of Conducting Polyaniline and of Conducting Polyblends of Polyaniline in Bulk Polymers, Synthetic Metals, Vol. 48, pp. 91-97.

[10] Alexandre, M., and Dubois, P. 2000, Polymer-Layered Silicate Nanocomposites: Preparation, Properties and Uses of a New Class of Materials, Materials Science Engineering, and R, and Vol. 28, pp. 1-63.

[11] Mott, C. J. B. 1988, Clay Cinerals-an Introduction, Catalysis Today, Vol. 2, pp. 199-208.

[12] Olad, A. 2011, Polymer/Clay Nanocomposites, Advances in Diverse Industrial Applications of Nanocomposites, Dr. Boreddy Reddy (Ed.), and ISBN: 978-953-307-202-9, InTech.

[13] Maiti, P., Yamada, K., Okamoto, M., Ueda, K., and Okamoto, K. 2002, New Polylactide/Layered Silicate Nanocomposites: Role of Organoclay, Chemistry of Materials, Vol. 14, and pp. 4654-4661.

[14] Tang, Z., Liu, P., Guo, J., and Su Z. 2009, Preparation of Polyaniline/Vermiculite Clay Nanocomposites by *in situ* Chemical Oxidative Grafting Polymerization, Polymer International, Vol. 58, pp. 552-556.

[15] Kalaivasan, N., and Shafi, S. S. 2010, Synthesis of Various Polyaniline/clay Nanocomposites Derived from Aniline and Substituted Aniline Derivatives by Mechanochemical Intercalation Method, E-Journal of Chemistry, Vol. 7, pp. 1477-1483.

[16] Garai, A., Kuila, B. K., and Nandi, A. K. 2006, Montmorillonite Clay Nanocomposites of Sulfonic Acid Doped Thermoreversible Polyaniline Gel: Physical and Mechanical Properties, Macromolecules, Vol. 39, pp. 5410-

5418.

[17] Song, D. H., Lee, H. M., Lee, K.-H. and Choi, H. J. 2008, Intercalated Conducting Polyaniline–clay Nanocomposites and their Electrical Characteristics, Journal of Physics and Chemistry Solids, Vol. 69, pp. 1383-1385.

[18] Kim, B. H., Jung, J. H., Hong, S. H., Joo, J. S., Epstein, A. J., Mizoguchi, K., Kim, J. W., and Choi, H. J. 2002, Nanocomposite of Polyaniline and Na^{+}-montmorillonite Clay, Macromolecules, Vol. 35, pp. 1419-1423.

[19] Yeh, J. M., Liou, S. J., Lai, C. Y., and Wu, P. C. 2001, Enhancement of Corrosion Protection Effect in Polyaniline via the Formation of Polyaniline-clay Nanocomposite Materials, Chemistry of Materials, Vol. 13, pp. 1131-1136.

[20] Nascimento, G. M. do, Constantino, V. R. L., and Temperini, M. L. A. 2002, Spectroscopic Characterization of New type of Conducting Polymer-clay Nanocomposite, Macromolecules, Vol. 35, pp. 7535-7537.

[21] Mansoori, Y., Hemmati, S., Eghbali, P., Zamanlooa, M. R., and Imanzadeh, G. 2013, Nanocomposite Materials Based on Ascribed Methacrylate/Cloisite 20A, Polymer International, Vol. 62, pp. 280-288.

[22] Panigrahi, M., Singh, N. K., Gautam, R. K., Banik, R. M., and Maiti, P. 2010, Improved Biodegradation and Thermal Properties of Poly (lactic acid)/Layered Silicate Nanocomposites, Composite Interfaces, Vol. 17, pp. 143-158.

[23] Crosa, M., Boero, V., and Franchini-Angela, M. 1999, Determination of Mean Crystallite Dimensions from X-ray Diffraction Peak Profiles: a Comparative Analysis of Synthetic Hematites, Clays Clay Miner, Vol. 47, pp. 742-747**.**

[24] Li, L., Qin, Z., Liang, X., Fan, Q, Lu, Y., Wu, W., and Zhu, M. F. 2009, Facile Fabrication of Uniform Core-shell Structured Carbon Nanotube-Polyaniline Nanocomposites, Journal of Physical Chemistry C, Vol. 113, pp. 5502-5507.

[25] Wu, T., Xie, T., and Yang, G. 2009, Characterization of Poly (vinylidene fluoride)/Na-MMT Composites: An Investigation Into the β-Crystalline Nucleation Effect of Na-MMT, Journal of Polymer Science, Part B: Polymer Physics, Vol. 47, pp. 903-911.

[26] Ciric-Marjanovic, G., Dondur, V., Milojevic, M., Mojovic, M., Mentus, S., Radulovic, A., Vukovic, Z., and Stejskal, J. 2009, Synthesis and Characterization of Conducting Self-assembled Polyaniline Nanotubes/Zeolite Nanocomposite, Langmuir, Vol. 25, pp. 3122-3131.

[27] Olad, A., and Rashidzadeh, A. 2008, Preparation and Anticorrosive

Properties of PANI/Na-MMT and PANI/O-MMT Nanocomposites, Progress in Organic Coatings, Vol. 62, pp. 293-298.

[28] Sengupta, P. P., Kar, P., and Adhikari, B. 2009, Influence of Dopant in the Synthesis, cCharacteristics and Ammonia Sensing Behavior of Pprocessable Polyaniline, Thin Solid Films, Vol. 517, pp. 3770-3775.

[29] Kapil, A., Taunk, M., and Chand, S. 2010, Preparation and Charge Transport Studies of Chemically Synthesized Polyaniline, Journal of Materials Science-Materials Electronics, Vol. 21, pp. 399-404.

[30] Li, J., Fang, K., Qiu, H., Li, S., and Mao, W. 2004, Micromorphology and Electrical Property of the HCl-doped and DBSA-doped Polyaniline, Synthetic Metal, Vol. 142, pp. 107-111.

[31] Ghosh, M., Barman, A., Meikap, A. K., De, S. K., Chatterjee, S., and Chattopadhyay, S. K. 2000, Electrical Resistivity and Magnetoresistivity of Protonic Acid (H_2SO_4 and HCl)-doped Polyaniline at Low Temperature, Journal of Applied Polymer Science, Vol. 75, pp. 1480-1486.

[32] Chakraborty, G., Gupta, K., Rana, D., and Meikap, A. K. 2012, Effect of Multiwalled Carbon Nnanotubes on Electrical Conductivity and Magnetoconductivity of Polyaniline, Advance in Natural Science, Nanoscience and Nanotechnology, Vol. 3, pp. 035015-035023.

[33] Kong, Y., and Hay, J. N. 2002, The Measurement of the Crystallinity of Polymers by DSC, Polymer, Vol. 43, pp. 3873-3878.

[34] Abdelkader, R., Amine, H., and Mohammed, B. 2012, Thermally Stable forms of Pure Polyaniline Catalyzed by a Acid-exchanged Montmorillonite Clay called Maghnite-H^+ as an Effective Catalyst, International Journal of Polymer Science, Vol. 2012, pp. 1-7.

[35] Zamboni, G., Capobianco, M., and Daminelli, E. 2009, Estimation of Road Vehicle Exhaust Emissions from 1992 to 2010 and Comparison with Air Quality Measurements in Genoa, Italy, Atmospheric Environment, Vol. 43, pp. 1086-1092.

[36] Hawe, E., Fitzpatrick, C., Chambers, P., Dooly, G., and Lewis, E. 2008, Hazardous Gas Detection using an Integrating Sphere as a Multipass Gas Absorption Cell, Sensors and Actuators A, Vol. 141, pp. 414-421.

[37] Richter, A., Burrows, J.P., Nuc, H., Granier, C., and Niemeier, U. 2005, Increase in Tropospheric Nitrogendioxide over China Observed from Space, Nature, Vol. 437 pp. 129-132.

[38] Jeong, O.C., and Konishi, S. 2008, Three-Dimensionally Combined Carbonized Polymer Sensor and Heater, Sensor and Actuators A, Vol. 143 pp. 97-105.

[39] Hoek, G., Brunekreef, B. Fischer, P., and Wijnen, J.V. 2001, The Association

Between Air Pollution and Heart Failure, Arrhythmia, Embolism, Thrombosis, and other Cardiovascular Causes of Death in a Time Series Study, Epidemiology, Vol. 12, pp. 355-357.

[40] Wierzbowska, K., Bideux, L., Adamowicz, B., and Pauly, A. 2008, A novel III-V Semiconductor Material for NO_2 Detection and Monitoring, Sensor and Actuators A, Vol. 142, pp. 237-241.

[41] Zamani, C., Shimanoe, K. and Yamazoe, N. 2005, A New Capacitive-Type No_2 Gas Sensor Combining An MIS with a Solid Electrolyte, Sensor and Actuators B, Vol. 109, pp. 216-220.

[42] Venema, A., Nieuwkoop, E., Vellekoop, M.J., Ghijsen, W.J., Barendsz, A.W., and Nieuwenhuizen, M.S. 1987, NO_2 Gas-Concentration Measurement with a SAW-Chemosensor, IEEE transection on Ultrasonic Ferroelectic Frequence Control, Vol. 34, pp. 149-156.

[43] Ricco, A.J. and Martin, S.J. 1991, Thin Metal Film Characterization and Chemical Sensors: Monitoring Electronic Conductivity, Mass Loading and Mechanical Properties with Surface Acoustic Wave Devices, Thin Solid Films Vol. 206 pp. 94-101.

[44] Auld, B.A. Acoustic Fields and Waves in Solid, New York: Wiley, 1973.

[45] Skotheim, T.A. Elsenbaumer, R.L. and Reynolds, J.R. Handbook of Conducting Polymers, 2nd ed., Marcel Dekker, New York, 1997.

[46] Anderson, M.R., Mattes, B.R., Reiss, H., and Kaner, R.B. 1991, Conjugated Polymerfilms for Gas Separations, Science, Vol. 252, pp. 1412–1415.

[47] Cao, Y., Smith, P., and Heeger, A.J. 1993, Counterion Induced Processibility of Conducting Polyaniline, Synthetic Metals, Vol. 57, pp. 3514-3519.

[48] Chiang, J.C., and MacDiarmid, A.G. 1986, Polyaniline-Protonic Acid Doping of the Emeraldine from to the Metallic Regime, Synthetic Metals, Vol. 13, pp. 193-205.

[49] Huang, W.S., Humphrey, B.D., and MacDiarmid, A.G.1986, Polyaniline, a Novel Conducting Polymer-Morphology and Chemistry of its Oxidation and Reduction in Aquwous-Electrolytes, Journal of the Chemical Society, Faraday Transections, Vol. 82, pp. 2385.

[50] Agbor, N.E., Petty, M.C., and Monkman, A.P., 1995, Polyaniline Thin-Films for Gas Sensing, Sensor and Actuators B: Chemical, Vol. 28 pp. 173-179.

[51] Kang, E.T., Neoh, K.G., and Tan, K.L. 1998, A Polymer with many Interesting Intrinsic Redox States, Progress in Polymer Science, Vol. 23 pp. 277-324.

[52] Huang, J.X., Virji, S., Weiller, B.H., and Kaner, R.B., 2003, Polyaniline Nanofibers: Facile Synthesis and Chemical Sensors, Journal of American

Chemical Society, Vol. 125 pp. 314-315.

[53] Huang, J.X., and Kaner, R.B. 2004 A General Chemical Route to Polyaniline Nanofibers, Journal of American Chemical Society, Vol. 126 pp. 851-855.

[54] Huang, J.X., and Kaner, R.B. 2004, Nanofiber Formation in the Chemical Polymerization of Aniline: A Mechanistic Study, Angewandte Chemie International Edition, Vol. 43 pp. 5817-5821.

[55] Ram, M.K., Yavuz, O., and Aldissi, M. 2005, NO_2 Gas Sensing Based on Ordered Ultrathin Films of Conducting Polymer and its Nanocomposite, Synthetic Metals, Vol. 151 pp. 77-84.

[56] H. Xu, D. Ju, W. Li, H. Gong, J. Zhang, J. Wang, B. Cao, 2016, Low-working-Temperature, Fast-Response-Speed NO_2 sensor with Nanoporous-SnO_2/Polyaniline Double-Layered Film, Sensor and Actuators B, Vol. 224 pp. 654-660.

[57] Yan, X., Han, Z.J., · Yang, Y.K.K., and Tay, B.K. NO_2 Gas Sensing with Polyaniline Nanofibers Synthesized by a Facile Aqueous/Organic Interfacial Polymerization, Sensor and Actuators B Chemical, Vol. 123, pp. 107-113.

[58] Kim, S.G., Jun, J., Lee, J.S., and Jang, J. 2019, A Highly Sensitive Wireless Nitrogen Dioxide Gas Sensor Based on an Organic Conductive Nanocomposite Paste, Journal of Materials Chemistry A, Vol. 7, pp. 8451-8459.

[59] Kumar, R., Singh, S., and Mishra, A.K. 2010, Development of NO_2 Gas Sensor Based on Plasma Polymerized Nanostructure Polyaniline Thin Film, Journal of Minerals & Materials Characterization & Engineering, Vol. 9, No.11, pp.997-1006.

[60] Surwade, S.P., Rao Agnihotra, S., Dua, V., and Manohar, S.K., 2009, Nitrogen Dioxide Vapor Detection using Poly-o-Toluidine, Sensor and Actuators B, 143, 454-457.

[61] Xie, D., Jiang, Y., Pan, W., Li, D., Wu, Z., and Li, Y. 2002, Fabrication and Characterization of Polyaniline based Gas Sensor by Ultrathin Film Technology, Sensor and Actuators B, Vol. 81, pp. 158-164.

[62] Rozemarie, M.L., Andrei, B., Liliana, H., Cramariuc, R. and Cramariuc, O. 2017, Electrospun Based Polyaniline Sensors – A Review, International Conference on Innovative Research — ICIR EUROINVENT 2017, IOP Conf. Series: Materials Science and Engineering Vol. 209, pp. 012063 (doi:10.1088/1757-899X/209/1/012063).

[63] Haynes, A., and Gouma, P.-I. Polyaniline-Based Environmental Gas Sensors, Sensors for Environment, Health and Securitypp, pp. 451-459.